HIFAN 1693

Heavy Ion Fusion Science Virtual National Laboratory 4th Quarter 2009 Milestone Report

Measure and simulate target temperature and dynamic response in optimized NDCX-I configurations with initial diagnostics suite

F.M. Bieniosek, J.J. Barnard, E. Henestroza, B.G. Logan, S. Lidia, R.M. More, P.A. Ni, P.A. Seidl
A. Friedman, D. Grote, and J.-L. Vay
Heavy Ion Fusion Virtual National Laboratory, Lawrence Berkeley National Laboratory, Berkeley, California 94720, USA

September 2009

Accelerator Fusion Research Division
Ernest Orlando Lawrence Berkeley National Laboratory
University of California
Berkeley, California 94720

This work was supported by the Director, Office of Science, Office of Fusion Energy Sciences, of the U.S. Department of Energy under Contract No. DE-AC02-05CH11231.

This work was supported by the Director, Office of Science, Office of Fusion Energy Sciences, of the U.S. Department of Energy under Contract No. DE-AC02-05CH11231.

HEAVY ION FUSION SCIENCE VIRTUAL NATIONAL LABORATORY

4th QUARTER 2009
MILESTONE REPORT

Measure and simulate target temperature and dynamic response in optimized NDCX-I configurations with initial diagnostics suite.

F.M. Bieniosek, J.J. Barnard, E. Henestroza, B.G. Logan, S. Lidia, R. M. More, P. A. Ni, P. A. Seidl, for the HIFS-VNL

September 30, 2009

1. SUMMARY

This milestone has been met. The effort contains two main components:

1. Experimental results of warm dense matter target experiments on optimized NDCX-I configurations that include measurements of target temperature and transient target behavior.

2. A theoretical model of the target response to beam heating that includes an equilibrium heating model of the target foil and a model for droplet formation in the target for comparison with experimental results.

The experiments on ion-beam target heating use a 300-350-keV K^+ pulsed beam from the Neutralized Compression Drift Experiment (NDCX-I) accelerator at LBNL. The NDCX-I accelerator delivers an uncompressed pulse beam of several microseconds with a typical power density of >100 kW/cm^2 over a final focus spot size of about 1 mm. An induction bunching module the NDCX-I compresses a portion of the beam pulse to reach a much higher power density over 2 nanoseconds. Under these conditions the free-standing foil targets are rapidly heated to temperatures to over 4000 K.

We model the target thermal dynamics using the equation of heat conduction for the temperature T(x,t) as a function of time (t) and spatial dimension along the beam direction (x). The competing cooling processes release energy from the surface of the foil due to evaporation, radiation, and thermionic (Richardson) emission.

A description of the experimental configuration of the target chamber and results from initial beam-target experiments are reported in our FY08 4th Quarter and FY09 2nd Quarter Milestone Reports. The WDM target diagnostics include a high-speed multi-channel optical pyrometer, optical streak camera, VISAR, and high-speed gated cameras. The fast optical pyrometer is a unique and significant new diagnostic which provides valuable information on the temperature evolution of the heated target.

2. INTRODUCTION

The US heavy ion fusion science program is developing techniques for heating ion-beam-driven warm dense matter (WDM) targets [1-4]. Intense ion beams have several attractive features as a technique for generating WDM. These features include:
-Precise control of local beam energy deposition dE/dx, nearly uniform throughout a given volume, and not strongly affected by target temperature,
-Large sample sizes (about 1 micron thick by 1 mm diameter),
-The ability to heat any target material, for example, foams, powders, conductors, insulators, solid, gas, etc.

The WDM conditions are achieved by combined longitudinal and transverse space-charge neutralized drift compression of the ion beam to provide a hot spot on the target with a beam spot size of about 1 mm, and compressed pulse length about 2 ns. The experiments use a 0.3 MeV, 30-mA K^+ beam (below the Bragg peak) from the NDCX accelerator to heat foil targets such as Au, Al and Si. The NDCX beam contains an uncompressed pulse length up to 20 μs with a peak energy flux >100 kW/cm^2, and a compressed pulse of fluence ~10 mJ/cm^2.

A detailed description of the experimental target chamber, targets, and target diagnostics was reported in the 3rd Quarter 2008 milestone report [1]. Initial target experiments in the new target chamber are described in the 4th Quarter 2008 Milestone Report. [5] Beam and target experiments and improvements in the induction bunching module, FEPS plasma, and target diagnostic and positioning equipment are described in the 2nd Quarter 2009 Milestone Report. The NDCX-I facility is show in Fig. 1.

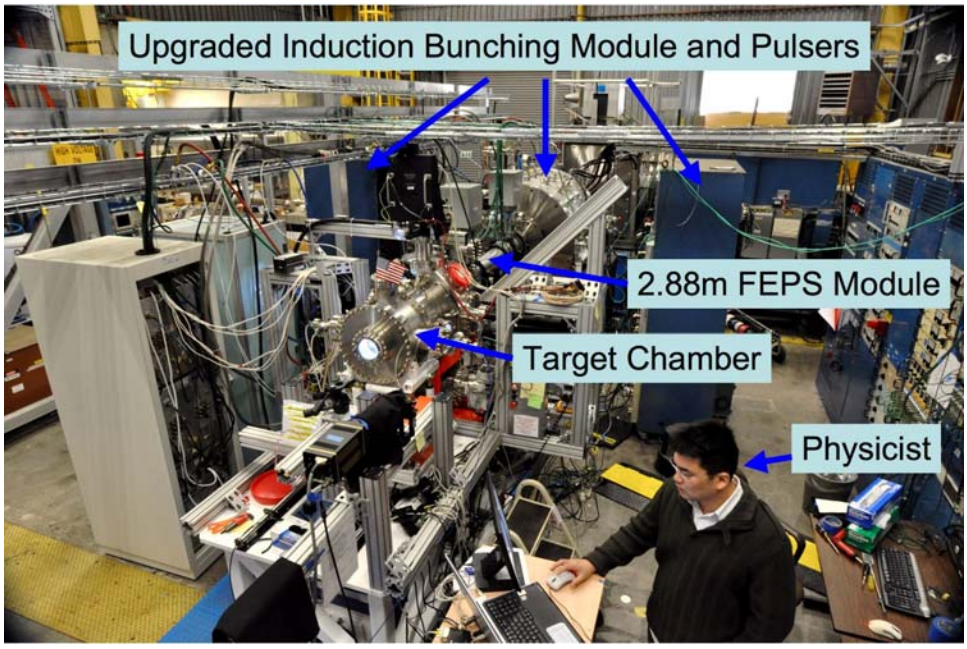

Fig. 1: NDCX-I beamline and facility.

3. NDCX CONFIGURATION AND BEAM PARAMETERS AT TARGET

As reported in the FY09 Q2 Milestone Report, we have improved the NDCX beamline and its capabilities for WDM studies. The improvements derive from the replacement of the original Induction Bunching Module (IBM) with a new one that can generate nearly twice the volt-seconds, and from a longer neutralized drift section that allows the longer duration energy modulated pulses to fully compress at the target plane.

The IBM waveform has been optimized for several operating beam energies. The waveform fidelity has improved so that the relative error in energy is less than 1% over ~400-500 ns pulse duration.

The temporal profile of the beam current is measured with a Faraday cup at the target plane that has ~1 ns response time. The beam energy is scanned to find the optimum operating conditions that produce the highest peak current and compressed pulse power and deposited energy. A secondary scan of the final matching solenoid field strength is performed to optimize the beam intensity and compressed pulse beam fluence.

We have employed several different IBM waveforms in our studies to optimize the compressed pulse intensity and ion beam fluence impinging upon the target foils. The optimal operating energy for each tune is determined empirically by scanning the uncompressed beam energy and observing the compressed pulse duration in the target chamber fast Faraday cup. The scans for the low and high energy bunching module tunes are shown in Fig. 2. The low energy tune displays a distinct minimum pulse length. The high energy tune is seen to approach or to find an optimum at the maximum safe operating voltage. The optimal energy displays some day-to-day variation due to small changes in the beamline length. The optimal energy found is used in all later measurements during that measurement period.

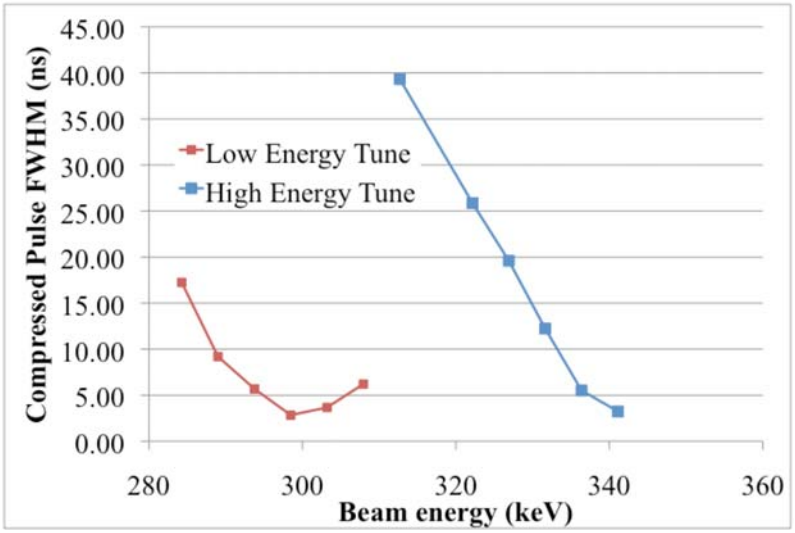

Fig. 2: Variation of compressed pulse duration (FWHM) with beam energy for the low energy (280-300 keV) and high energy (330-340 keV) tunes.

Compressed beam intensity and fluence

The delivered beam intensity and fluence for the compressed pulse has been derived from the long duration (500ns) gated image and beam current measurements from the fast Faraday cup. The former describe the transverse intensity distribution that has been integrated over the gate pulse duration (i.e. 500 ns), while the latter provide a normalization of the charge included in the compressed peak, compared to the total charge included in the long duration (500 ns) gate window.

Once the optimal beam energy is determined, the transverse beam distribution is collected optically by a fast, gated, image-intensified MCP camera (Princeton Instruments PI-Max) from the fluorescence emission of the beam impacting on a 100 µm thick alumina scintillator. After subtracting a background image, each beam image is cropped and further processed to remove stochastic noise and any residual flat background level. An averaging filter is applied last to simulate the averaging effect of the 400µm diameter optical fiber in the target diagnostic light acquisition system.

The beam spot size and peak intensity is measured as a function of the field strength of the final matching solenoid (located upstream from the IBM). A typical scan for the low energy case is shown in Fig. 3 for the uncompressed beam. Measuring the uncompressed region of the beam fixes the intensity of the prepulse striking the target prior to the compressed pulse arrival.

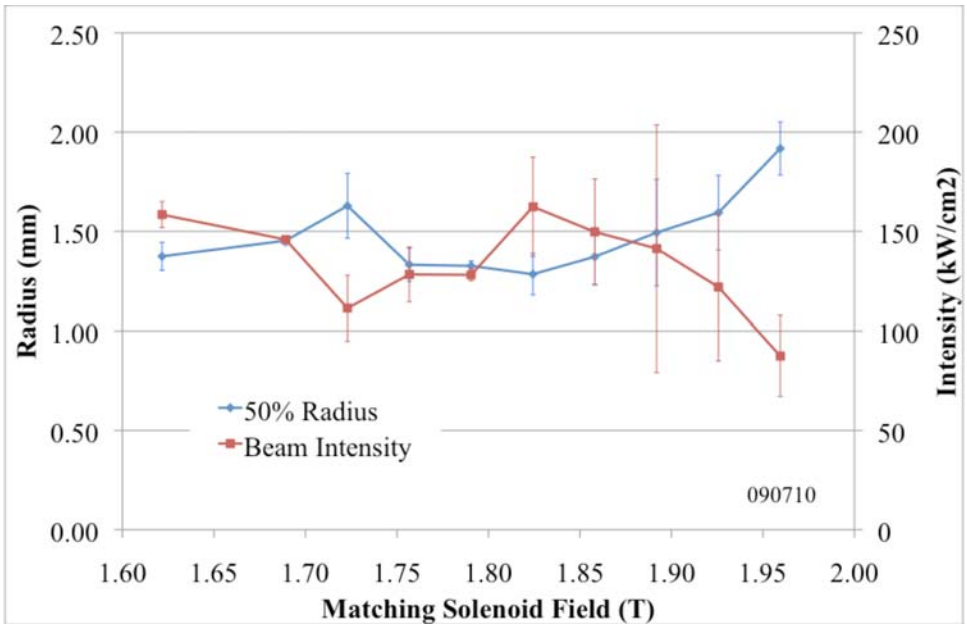

Fig. 3: Matching solenoid tune scan for the low energy, uncompressed beam.

The uncompressed beam scintillator images for the low and high energy cases are shown in Figs. 4 and 5. The intensities are calculated from the measured beam current and energy, and the images are acquired over a 500-ns gate window. The high energy case is seen to optimize to a somewhat larger spot size at the target plane. This is due, primarily, to the high field limitation of the final focus solenoid (~8T) and the fixed drift length between it and the target plane. The system is designed to be well matched for the lower energy beams. The high energy case is likely to not be jointly focused in both transverse and longitudinal phase spaces. The smaller achievable spot sizes in the low energy case directly influence the observed larger peak intensities. The uncompressed beam parameters are tabulated in Table 1.

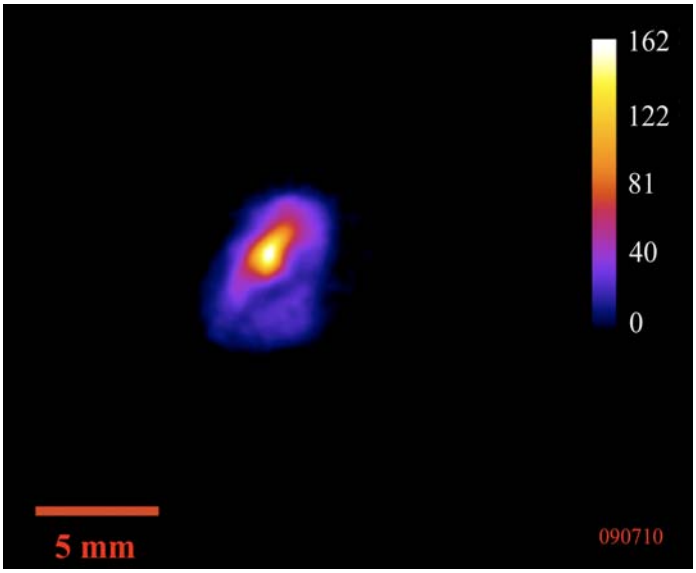

Fig. 4: Intensity map (in kW/cm^2) of the low energy, uncompressed beam.

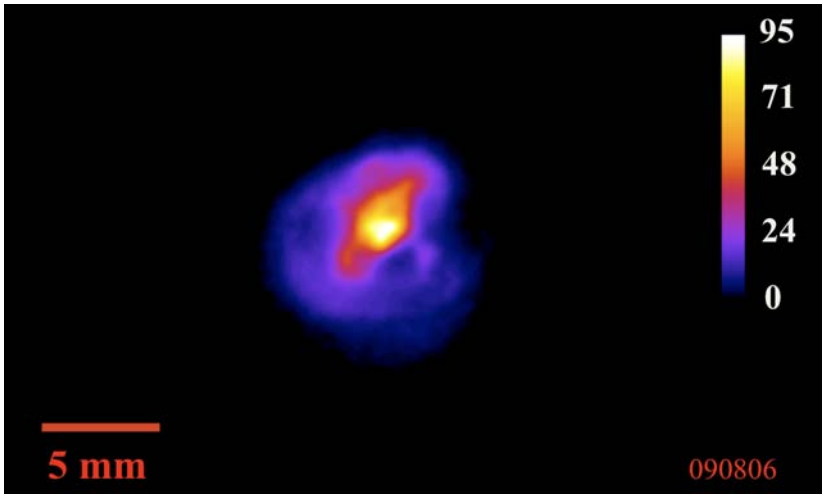

Fig 5: Intensity map (in kW/cm^2) of the high energy, uncompressed beam.

Table 1: Uncompressed beam parameters

	Low Energy Tune	High Energy Tune
Beam Voltage (kV)	298	341
Beam Current (mA)	27.2	33.1
Beam Power (kW)	8.1	11.3
Matching Solenoid Field (T)	1.82	2.06
50% Intensity Radius (mm)	1.28	1.90
Peak Intensity (kW/cm^2)	162	95

The peak intensities list in Table 1 for the uncompressed beam are lower than those reported in our FY09 Q2 Milestone report. Several systematic errors in the data reduction and analysis process have been identified and removed. These errors had artificially raised the peak intensity and fluences observed. Additionally, the process of filtering the intensity distribution to account for the effect of averaging over the optical fiber diameter further depresses the peak intensity value.

Compressed beam images are shown in Figs 6 and 7 for the low and high energy cases, respectively. Theses images are normalized similarly to the uncompressed images. However, an assumption is made that the transverse distribution is similar between the 500 ns gate case and a gate window duration that only encloses the compressed peak. With this assumption, the image peak intensities then scale with the beam current ratio between the uncompressed beam and the compressed peak. Similarly to the uncompressed case, we observe somewhat lower peak intensities and larger beam sizes in the higher energy case than in the lower energy case.

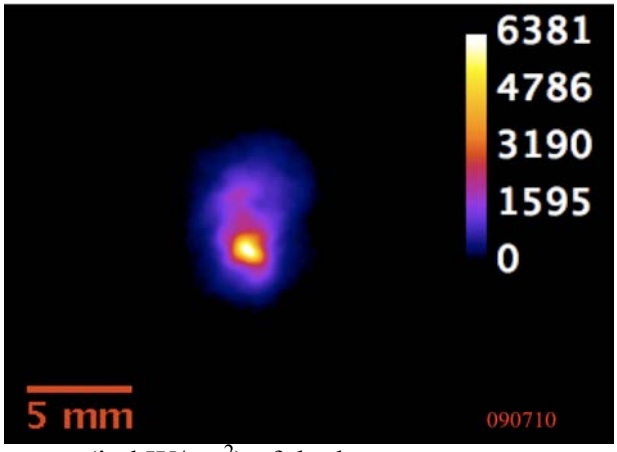

Fig. 6: Intensity map (in kW/cm^2) of the low energy, compressed beam pulse.

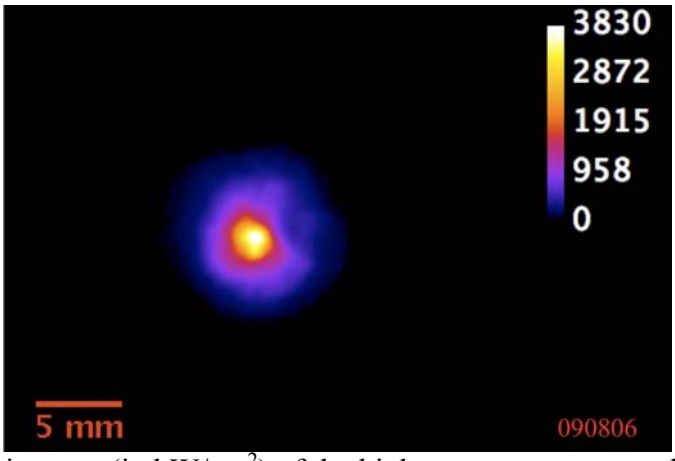

Fig. 7: Intensity map (in kW/cm^2) of the high energy, compressed beam pulse.

The compressed beam fluence distribution is also derived from the temporal profile of the beam current and the optical record of the transverse beam distribution. The peak beam fluence for the compressed pulse (3-4-ns FWHM) is obtained from the 500-ns gate window duration image by scaling the ratio of charge in the compressed peak to the charge in the 500-ns duration gate window. The compressed beam parameters are tabulated in Table 2.

Table 2: Compressed beam parameters.

	Low Energy Tune	High Energy Tune
Beam Voltage (kV)	298	341
50% Intensity Radius (mm)	1.48	1.84
Peak Beam Power (kW)	479	594
Pulse Duration, FWHM (ns)	3.8	2.9
Pulse Charge in FWHM (nC)	4.2	3.8
Pulse Energy in FWHM (mJ)	1.25	2.2
Peak Intensity over FWHM (kW/cm^2)	6381	3830
Peak Fluence over FWHM (mJ/cm^2)	24.5	11.2

4. TARGET POSITIONER AND DIAGNOSTICS

As noted above, detailed descriptions of the experimental target chamber, targets, and target diagnostics were reported in several recent milestone reports, including the 3rd Quarter 2008 milestone report [1], the 4th Quarter 2008 Milestone Report. [5] and the 2nd Quarter 2009 Milestone Report.

Previously-described target diagnostics include the fast optical pyrometer, an optical streak-spectrometer, two high-speed gated image intensified cameras. In addition the completion of the precision target positioning equipment allows rapid re-positioning of the target foil between shots. Using this positioning equipment, we have been able to reduce the shot-to-shot repetition time to as little as 4 minutes.

We have installed a new current monitor downstream of the target. This current monitor is a Bergoz FCT-016-20:1-VAC fast current transformer with a 20:1 turns ratio. The purpose of the current monitor is to measure beam current transmitted through the target as a function of time. In a target thicker than the range of the beam, the beam current transmitted should be small even as the target vaporizes since the beam stopping for solid and vapor target material is very similar. This is the case if no droplets form in the target. However if and when the target bunches up into droplets we expect to see a change in transmitted beam current. Sample data from this new diagnostic is described later in this report.

Improvements to the target assembly include the installation of a simple final focus cone. The cone has a 4-mm entrance aperture, 1-mm exit aperture, and a pitch angle of 200 mrad. The cone enhances beam intensity on target by reflecting additional beam ions that are initially radially outside the target area. In addition to enhanced flux, other expected advantages of the cone include: 1. An additional source of electrons from ion collisions with the cone for space charge neutralization at the target; 2. Reduced beam space potential because of the close proximity of the metal cone wall to the beam; and 3. Improved uniformity of beam energy flux on target because of the presence of reflected ions among the beam ions striking the target.

Fig. 8 shows a platinum target after a number of shots were taken on the foil. The target manipulator was used to reposition the target between shots. Up to 40 beam shots were taken per day with a repetition rate of as little as 4 minutes. A total of 69 beam-target shots were taken using this foil before it was removed from the target chamber and replaced with a fresh foil.

Fig. 8. Target holder containing a platinum target foil (above) and a small scintillator (below).

5. MODEL OF TARGET DYNAMICAL RESPONSE

A. Equilibrium target heating model

As the ion beam deposits the energy volumetrically on the solid target, initially at room temperature, the target goes through a series of phase changes depending on the total beam energy fluence and power. For the beam power density levels available in NDCX-1, in the 100 kW/cm^2 range for the longitudinally uncompressed beam (for several μs), and in the >> 1 MW/cm^2 range for the longitudinally compressed beam (for 2 ns) the target will go through a melting process and vaporize a fraction of its mass reaching temperatures near 0.5 eV (~ 6000 K). Since this beam power level is not enough to substantially ionize the target, we don't expect to observe the formation of a plasma.

A complete numerical modeling would include the dynamics of the target as it progresses in time through the solid, liquid and gas states. Since the diagnostics used in NDCX-1 can measure the temperature of the condensed (liquid and solid) state of the target through the low-density vapor, it is possible to reduce the description of the target dynamics to the study of the time dependence of the surface temperature during and after the passage of the ion beam.

NDCX-1 can compress the beam spot size to a radius of about 1 mm. The targets are thin foils less than a micron in thickness. The diffusivity of these targets of order 1 cm^2/s or less, which means that even for the 10-μs pulse time scale the heat diffuses transversely by less than 30 microns. Therefore we can model the target dynamics using only time and the spatial dimension along the beam direction. The equation of heat conduction for the temperature T(x,t) is

$$\rho c_p \frac{\partial T}{\partial t} = \frac{\partial}{\partial x}\left(K \frac{\partial T}{\partial x} \right) + S(x,t),$$

where ρ, c_p and K are the density, the specific heat at constant pressure, and thermal conductivity which may be functions of temperature and position; S(x,t) is an external source of heat which in our case is the heat generated by the ions deposited in the target. The initial condition is T(x,t=0) = T_0 where T_0 = 293 K. The boundary condition on the surface of the foil (both sides) is given by

$$\left(K \frac{\partial T}{\partial x} \right)_{L,R} = F_{L,R}(T),$$

where $F_{L,R}$ is the (left and right) energy flux off the surface of the foil due to evaporation, radiation, and thermionic (Richardson) emission; Joule (resistive) heating from the electron current is neglected. Note that F_R=-F_L≡F(T)= Fv(T)+Fr(T)+Ft(T) and that the boundary is moving because the foil evaporates continuously.

The thermal radiation energy flux is given by $Fr(T)=\varepsilon s T^4$, where s is the Stefan-Boltzmann constant and ε is the emissivity of the target (~ 0.1 — 0.4). The thermionic electron energy flux is given by $Ft(T)=120\ T^2\ W\ Exp(-W/kT)$, where k is the Boltzmann constant and W is the thermionic work function of the target. The energy flux from evaporation can be calculated approximately from the vapor pressure P_v if we assume that the vapor is an ideal gas:

$$F_V(T) = \alpha L_V \frac{P_v}{\sqrt{2\pi MRT}},$$

where L_v is the latent heat of vaporization per mol, M is the molar weight of the target and R is the Gas constant. The factor α~1, called the accommodation coefficient, comes from the fact that the rate of evaporation depends on properties of the target surface, similar to the emissivity factor in the thermal radiation formula. The vapor pressure as function of temperature can be obtained either from tabulated values (CRC Handbook of Chemistry and Physics) or from the Clausius-Clapeyron equation; we have chosen to use data from CRC tables. (From the Clausius-Clapeyron equation the expression for the vapor pressure is given by

$$P_V = P_0 * e^{-L_V *(1/T - 1/T_{boil})/R},$$

where $P_0 = 1\ atm$, and T_{boil} is the boiling point.)

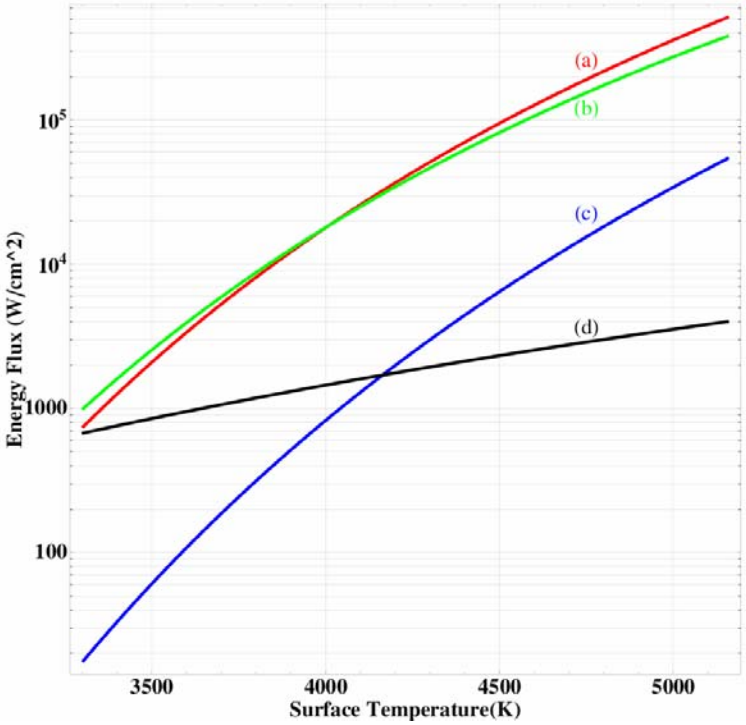

Fig. 9. Energy flux from cooling mechanisms in the equilibrium model for Pt.

Figure 9 shows the relative importance of each of the cooling mechanisms as a function of surface temperature. Curve (a) corresponds to the energy flux from evaporation as calculated using data from the CRC tables; curve (b) is also the energy flux from evaporation but calculated using the Clausius-Clapeyron equation; curve (c) corresponds to the energy flux from Richardson cooling; and curve (d) is the energy flux thermal radiation.

Using this model we calculate the temperature at which the cooling mechanisms equilibrate the energy flux from the ion beam (Fig. 10). NDCX-I delivers beam intensity sufficient to reach equilibrium temperatures in the range of 3000 to 6000 K.

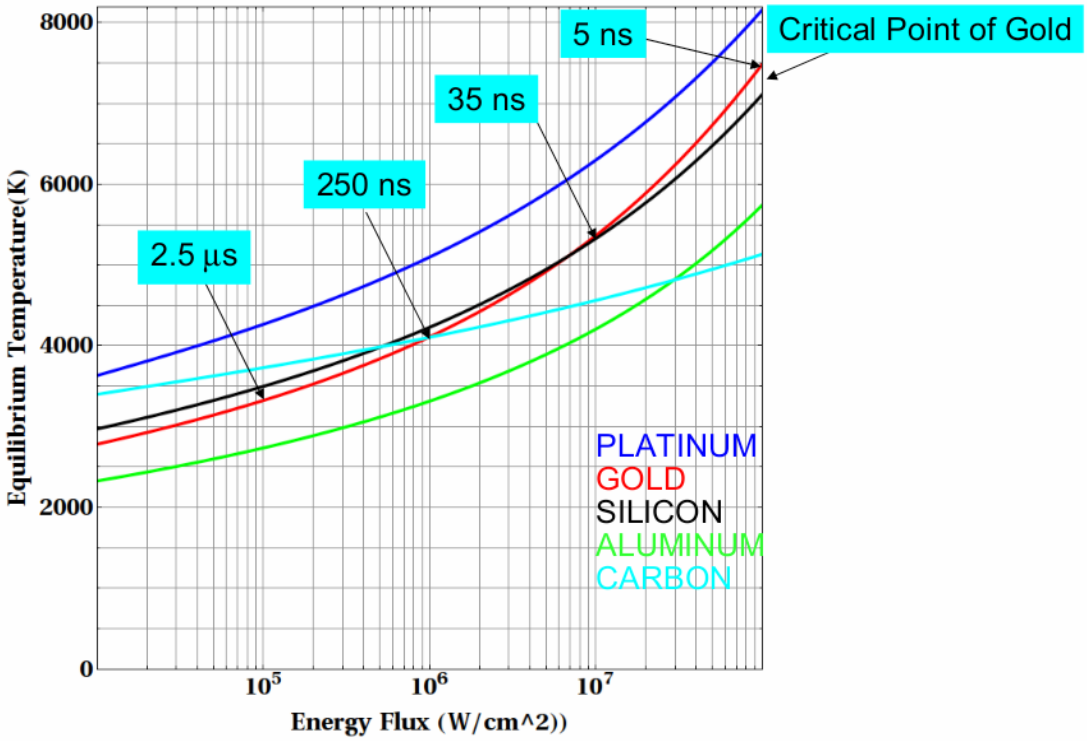

Fig. 10. Equilibrium temperature as a function of beam energy flux. Times indicated refer to time needed to reach equilibrium temperature.

The temperature dependence of the density and thermal conductivities are obtained from CRC tables. The temperature dependence of the molar specific heat is calculated from the Debye equation

$$c_v(T) = 9R(T/T_D)^3 \int_0^{T_D/T} \frac{x^4 e^x}{(e^x - 1)^2} dx.$$

Only carbon targets (T_D=2230 K) have a strong dependence of the specific heat on temperature in the range considered for the NDCX-1 target experiments Also, since we are modeling only the condensed state of the target, we can neglect the thermal expansion

and obtain $c_p \sim c_v$. For all the other targets the molar specific heat at constant pressure is $c_p \sim 3R$.

The target temperature reaches an equilibrium within a time on the order of 1 μs. The temperature then slowly falls as the target becomes thinner due to vaporization from the front and rear surfaces. The calculation is based on the energy deposition model of the TRIM code. Figs. 11 and 12 show the time dependence of the surface temperature and the target thickness for several targets assuming uncompressed beam energy flux of 500 kW/cm^2. The thickness of each target is: Gold: 150 nm, Aluminum: 350 nm, Platinum: 120 nm, Silicon: 400 nm, and Carbon: 400 nm. As predicted by the equilibrium temperatures shown in Figure 10, the targets reach temperatures between 3000 K and 5000 K. Note that in this model, the gold and platinum targets are completely vaporized in a 4-μs pulse, whereas the carbon target loses only a small fraction of its mass, due to its lower vapor pressure.

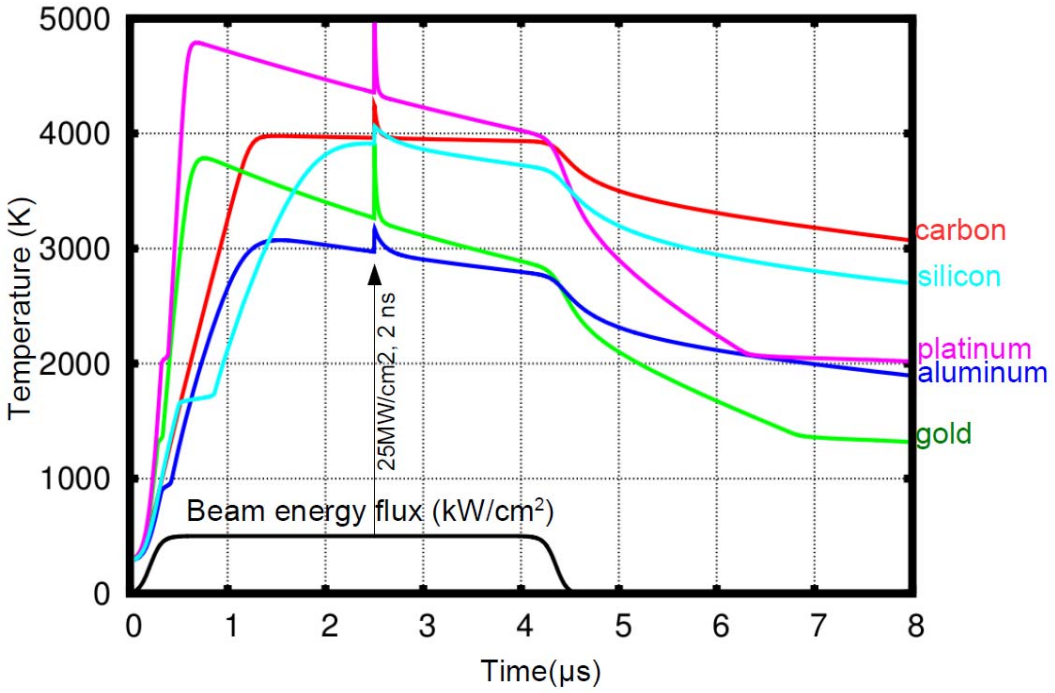

Fig. 11. Target temperature as a function of time for idealized 4-μs uncompressed and 2-ns compressed beam pulse as shown.

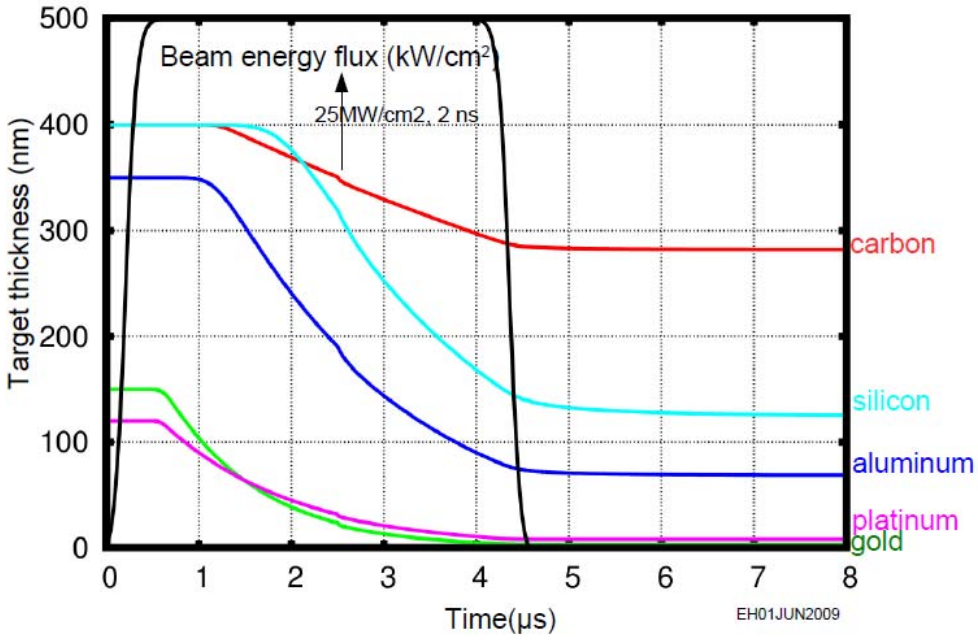

Fig. 12. Target thickness as a function of time for the same beam pulse as in Fig. 3.

To check the sensitivity of the thermal dynamics of the target on some of the simulation parameters or assumptions, we show in the Fig. 13 three temperature profiles for calculations i) taking the vapor pressure form the CRC tables, ii) calculating the vapor pressure from the Clausius-Clapeyron equation, and iii) assuming an accommodation coefficient α=0.9, where the other curves were calculated using α=1. Note the weak dependence of the temperature profiles on relatively large changes of simulation parameters.

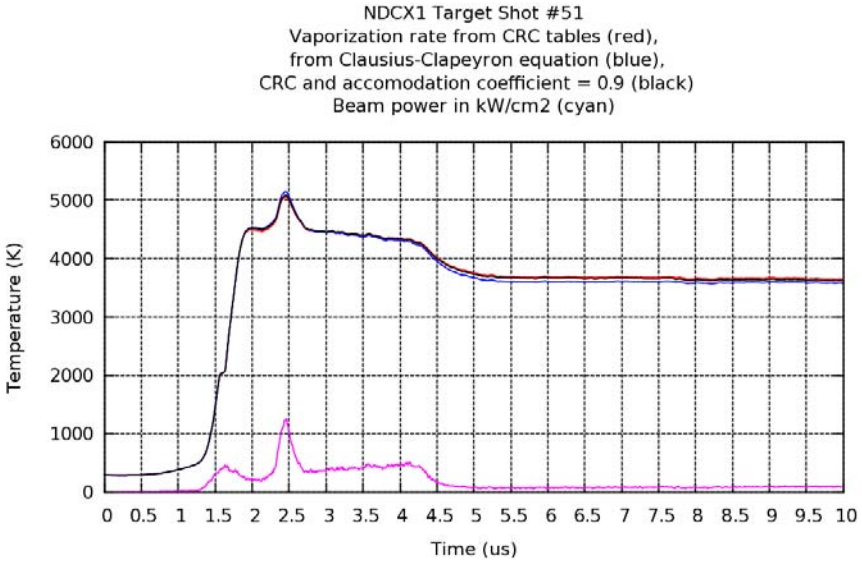

Fig. 13. Sensitivity of heating model to some parameter assumptions.

B. Dynamic processes and droplet formation

One of the key areas of investigation in warm dense matter is the dynamic transition between liquid and vapor of superheated metals. In particular, as the solid is heated above the melting temperature it first enters a liquid state (or if the temperature is high enough -- above the critical point-- it enters a fluid state that could be considered either liquid or vapor). In NDCX I, the temperature reached in metals such as gold and aluminum places it in a liquid state. As discussed above, the foil reaches a quasi-equilibrium, which is a balance between heating by the beam and cooling by evaporation and electron emission. As the pressure builds in the foil, expansion will occur, and droplets will form, due to surface tension effects. A complete theory of precisely how these droplets form is lacking but we have physical arguments and quantitative estimates that suggest that they should form. In addition we now have experimental evidence for droplet formation from three independent optical measurements:

1. The first indication that droplets form comes from the intensity measurements of the gold foil. During beam heating of the foil, after approximately 2 μs, the light intensity begins to decrease. One explanation for this effect is the reduction in projected surface area, as the ~200 nm foil breaks up into ~ 1000 nm radius droplets. The reduction in light intensity corresponds to the reduction in projected surface area.
2. The most direct measurement of the droplets, are photographic images of several hundred point sources of light expanding at a speed of a few meters/sec, that have been obtained from the Au and Pt foils. Although the size of the droplets is below the resolution of the camera, if we assume the mass of the heated part of the foil is converted into droplets, then the quantity of droplets implies that size of the droplets is on the order of a micron.
3. The third area of evidence is the dynamic change in the spectrum of the foil. Roughly at the time that the intensity decreases (after ~ 2 or 3 μs) the intensity at wavelengths longer than about 600 nm begins to decrease, whereas the intensity below that wavelength remains constant. If the droplets are smaller than the wavelength of light they will be poor radiators, and so the wavelength at which the spectrum begins to turn over is an indicator of the droplet scale size. Not all of the targets tested, have been observed to display all of these characteristics. We summarize the data in Table 3.

Table 3. Summary of optical observations giving evidence for droplet formation

Target	Foil Thickness (nm)	Optical intensity decrease after 2-3 μs?	Imaged, expanding point light sources?	Roll off of spectra at ~ 3 μs at $\lambda >$ 0.6 μm?
Gold	150	yes	yes	yes
Aluminum	350			
Platinum	120	yes	yes	yes
Carbon	400	yes		

A fourth area of evidence (not included in the table above) is based on preliminary analysis of the current transformer data. The current transformer shows a rapid increase

in signal level at about 2 μs into the beam pulse, suggesting breakup of the target into droplets at about this time. When the target bunches up into droplets, much of the incident beam current can pass through the target to be detected by the current transformer downstream of the target.

Droplets are predicted to form because of a proposed instability in targets which are thicker than the range of the beam. The instability is driven by the surface tension of the liquid metal foils, which are 0.1 – 0.4 μm thick. The basic mechanism is that the dependence of surface tension on temperature is negative, i.e. $d\sigma/dT < 0$, where σ is the surface tension of the liquid metal foil after it has become liquid. In what is known as the Marangoni effect, a liquid with higher surface tension pulls more strongly on the surrounding liquid than one with a lower surface tension. The gradient in the surface tension causes the liquid to flow away from regions of low surface tension. In a target foil, natural variations in the thickness of the foil can be expected to cause transverse local variations in the temperature of the foil across its face. For the situation in which the beam range is shorter than the thickness of the foil, and in which the thermal diffusion time over the distance of the thickness of the foil is much less than the heating time, the temperature will be highest where the foil is thinnest. The time required to melt the foils is an important consideration in determining the transverse distance over which the foil can thermally equilibrate before it becomes liquid. It depends on the rate of beam heating and on the thermal diffusivity of the target material. The ratio of the thermal diffusivity to the heating rate determines the characteristic transverse scale length over which the foil can equilibrate before melting. Once the foil melts, temperature variations over the surface of the foil, which do not have time to equilibrate, cause transverse flow of liquid target material. The liquid metal flows from the hotter regions which are relatively thin to the cooler regions which are relatively thick. This effect sets up a positive feedback loop which rapidly increases the variations in target thickness across the foil surface. The variations grow over time until the thicker portions of the target separate and form droplets.

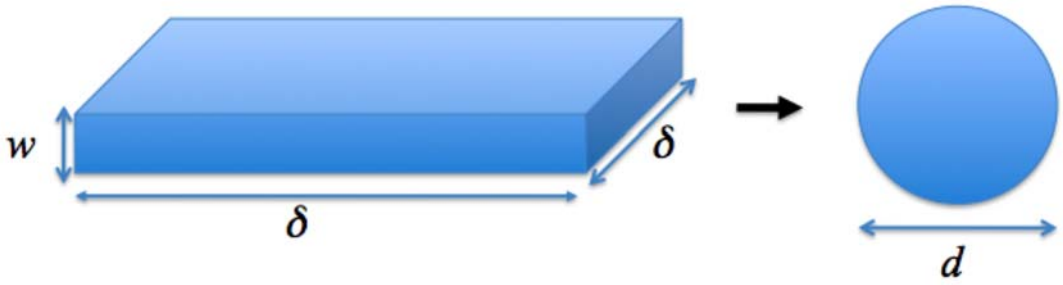

Fig. 14. Geometry of assumed square patch of foil that transforms into a spherical droplet due to differential surface tension.

The surface tension of liquids in general falls from its maximum at the melting point to zero at the critical point. As a result if the target is heated beyond the critical point this instability has no significance. Assuming a linear dependence on temperature, the surface tension scales with temperature T as $d\sigma/dT = -\sigma_0/T_C$, where T_c is the critical

temperature and σ_0 is the surface tension of a cold target. If the fluctuation in the thickness of the target is 1 part in 100 over the relevant scale length, then the resulting 1% temperature fluctuation leads to a fluctuation in the surface tension of .01 $\Delta T/ T_c$, or if the ratio of T/ T_c is 0.3, about .003. The time scale τ to form a droplet can be estimated in several ways. If w is the foil thickness, and δ is the length of a side of a square patch of the foil that will form a spherical droplet of diameter d (see Fig. 14), then the difference in surface area between square patch and sphere is $\Delta S = 2\ \delta^2 - \pi\ d^2$, and the potential energy difference due to surface tension is $\Delta E \approx \sigma\ \Delta S$. If the surface tension gives rise to a velocity $(\delta - d)/\ \tau$, then equating kinetic to potential energy, implies a time scale

$$\tau = \left(\frac{\rho w \delta^2}{2\sigma}\right)^{1/2}\left(\frac{(\delta - d)^2}{2\delta^2 - \pi d^2}\right)^{1/2} \approx \frac{1}{2}\left(\frac{\rho w \delta^2}{\sigma}\right)^{1/2}.$$

Here the final approximate equality holds when $\delta >> d$, which is generally the case. Another way of making this estimate is to examine the timescale for a droplet to make an oscillation about an equilibrium radius $d/2$. For on oscillating ellipsoidal droplet with initial polar radius $w/2$ and equatorial radius $\delta/2$, such that $d = (w\delta^2)^{1/3}$, the time for one quarter of an oscillation period (i.e. the time to go from maximum radius to a spherical shape) is [6]

$$\tau = \frac{\pi}{16}\left(\frac{\rho w \delta^2}{\sigma}\right)^{1/2}$$

Both estimates give the same scaling with a numerical coefficient differing by a factor ~2.5.

Table 4. Typical parameters for estimating droplet dynamics and sizes

Parameter	Symbol	Units	Au	Al	Si	Pt	Comments
Initial foil thickness	w	μm	0.15	0.35	0.40	0.12	
Density	ρ	g/cm^3	19.3	2.7	2.33	21.5	
Thermal diffusivity	α	cm^{2}s	1.3	1.0	0.9	0.25	
Melt time	t_m	μs	0.38	0.62	1.7	0.60	(at 150 kW/cm^2)
Length of side of initial square	δ	μm	7.0	7.8	12.5	3.9	Maximum scale determined by thermal diffusion $\delta=(\alpha t_m)^{1/2}$
Equilibrium diameter of droplet	d	μm	2.4	3.4	4.9	1.5	$d= (6\ \delta^2 w/\pi)^{1/3}$
Surface tension	σ	J/m^2	1.1	1.0	0.8	1.8	(At melting temperature)
Timescale for droplet formation	τ	μs	0.7	0.5	0.8	0.3	$\tau=(\pi/16)(\rho w\delta^2/\sigma)^{1/2}$

If the initial perturbation in surface tension is in the range 0.01 to 0.001 then formation of spherical droplets takes place over about 5-10 e-folding times, or 5-10 τ. This estimate assumes exponential growth typical of a linear instability. Our initial attempt to mathematically model this instability with an ideal fluid has found that the perturbation in thickness multiplies the perturbation in surface tension, yielding a *linearly* stable equation but nevertheless offers the possibility of non-linear instability. Work continues on a more rigorous mathematical description of the heuristic argument presented here.

As indicated above, the droplets are expected to be ellipsoidal in shape and to oscillate through a minimum size since the viscosity of the liquid metal is rather low. The low damping factor due to viscosity leads to underdamped oscillations of the droplets. However mixing is expected from asymmetries arising in the process of droplet formation. These processes should damp the oscillations much faster than might be expected from the rather weak viscosity effects.

The diameter of the resulting liquid droplet is related to the size of the initial patch of the target foil that it came from. That diameter is obtained by equating the volume of the foil and the spherical droplet, $d = \left(\frac{6}{\pi}\delta^2 w\right)^{1/3}$. The ratio of surface areas of the spherical droplet to the original foil is $R = \left(\frac{9\pi}{2}\frac{w^2}{\delta^2}\right)^{1/3}$. The ratio R = 1 occurs at $\delta/w = (9\pi/2)^{1/2} \approx$ 3.8. Thus there is a lower limit to the transverse size of the fluctuations that can cause a breakup of the target; the formation of droplets due to surface tension below this transverse size is not energetically favorable since the resulting spherical droplets have a surface area larger than the original foil for transverse scale smaller than about 3 to 4 times the foil thickness. For comparison the first estimate above for the droplet formation time yields for $\tau = \infty$, w/d = 3.

The characteristic transverse size can be estimated by comparing the rate at which thermal fluctuations are equilibrated by thermal conduction in the bulk of the foil and the rate at which the foil is heated to the melting temperature. If the heating time is given by t_h, then the transverse scale is simply $\delta = \sqrt{\alpha t}$ where α is the thermal diffusivity, typically around 1 cm^2/sec for most metals. These scaling relations taken together provide a quantitative basis for a model of liquid droplet formation. Table 2 shows a summary of the model estimates for several target materials.

The model has several predictions which can be tested, including the spectrum of droplet sizes, droplet formation times, and stabilization effect of increasing beam power or foil thickness less than beam range. The droplets can be collected by foil or aerogel for analysis of droplet size, penetration, and angular distribution of the collected droplets. The increasing surface roughness which proceeds droplet formation may be diagnosed using optical diagnostics such as observation of the emissivity of the target at a non-normal viewing angle.

We are beginning to compare detailed theory that describes the emission spectrum from Droplets. We use handbook values for the room-temperature optical constants and assume these do not change significantly at the temperature of the experiments. The calculation (Fig. 15) is done by extending the textbook Mie scattering theory to a general dielectric function and adapting it to calculate absorption and emission coefficients for the droplets. For droplets at a radius of 0.1 micron the emission has qualitative features suggestive of the data (including the decreased emission at long wavelengths). However, at a droplet radius of 0.2 microns the spectrum is quite different, suggesting that these spectral measurements may be sensitive indicators of droplet size. This work is in progress.

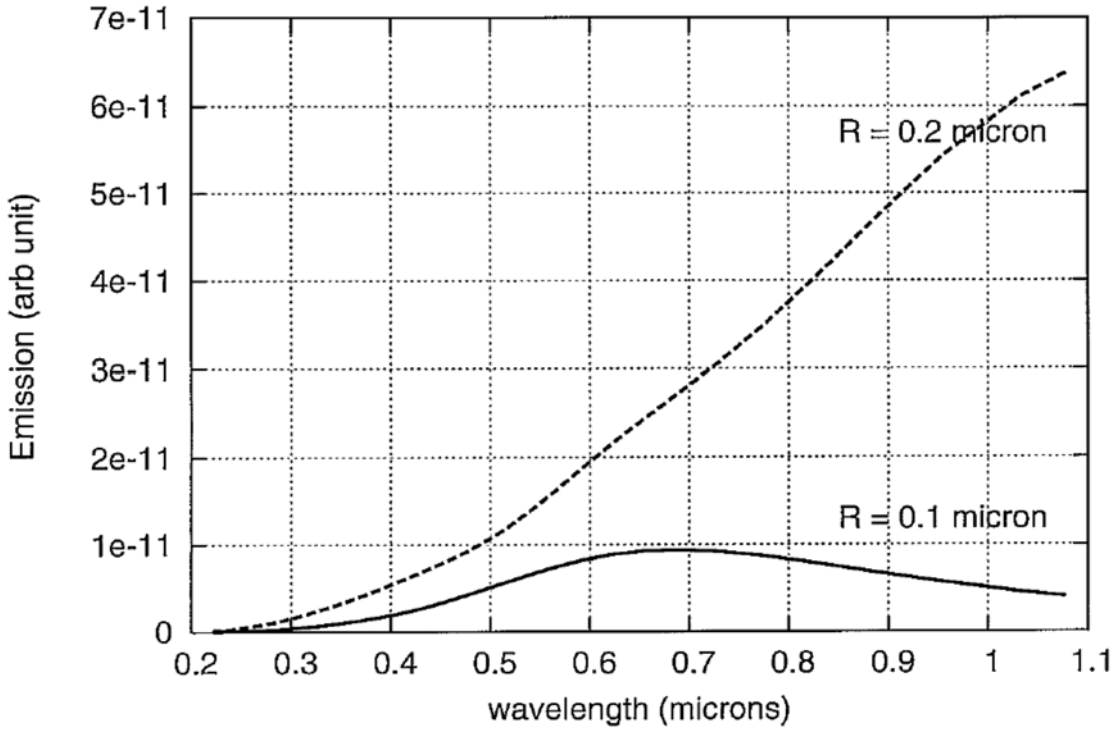

Fig. 15. Calculated optical radiation from a spherical platinum droplet at a temperature of 0.5 eV for two cases of droplet radius.

6. EXPERIMENTAL BEAM - TARGET DATA

NDCX-I beam-target shots have been performed on gold, platinum, carbon, aluminum and silicon targets. Typical experimental results for some of these targets are described below. Optical data was taken using gated ICCD cameras, the streak spectrometer, and the fast optical pyrometer diagnostic.

Carbon

Fig. 16 shows a gated camera image of a carbon target foil during a beam heating experiment. The diameter of the pinhole is 1 mm. The image shows that the fireball of hot carbon expands during the first 6 μs from the beam pulse to >2 mm, more than twice the initial diameter of the heated region.

Figs. 17 and 18 show results from the streak-spectrometer diagnostic. These results indicate a peak reconstructed target temperature of 4000 K. The peak temperature agrees with the heating model prediction (Fig. 11). However there is a rapid drop in corrected temperature at t = 3 μs which is not predicted in the model. Since carbon is not expected to form liquid droplets, we interpret this result to indicate formation of a cloud of hot carbon debris, as imaged in Fig. 16.

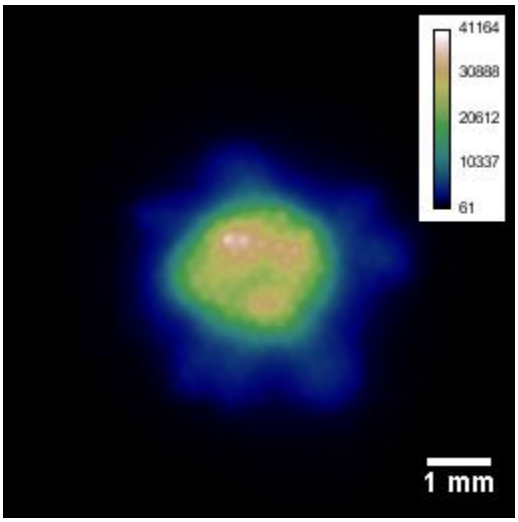

Fig. 16. Gated camera image (gate width = 6 μs) of a carbon target foil heated by a NDCX beam pulse.

Reconstructed temperature, T, is obtained from non-linear least square fit of experimental spectra, I(λ,T) to a radiation model. The model is the Planck formula multiplied by emissivity, ε(λ,T), which is depending on situation, has either linear or square dependence on wavelength [7].

$$\mathrm{I}(\lambda, \mathrm{T}) = \varepsilon(\lambda) \cdot \frac{\mathrm{C}_1}{\lambda^5} \frac{1}{e^{\frac{\mathrm{C}_2}{\lambda \mathrm{T}}} - 1}.$$

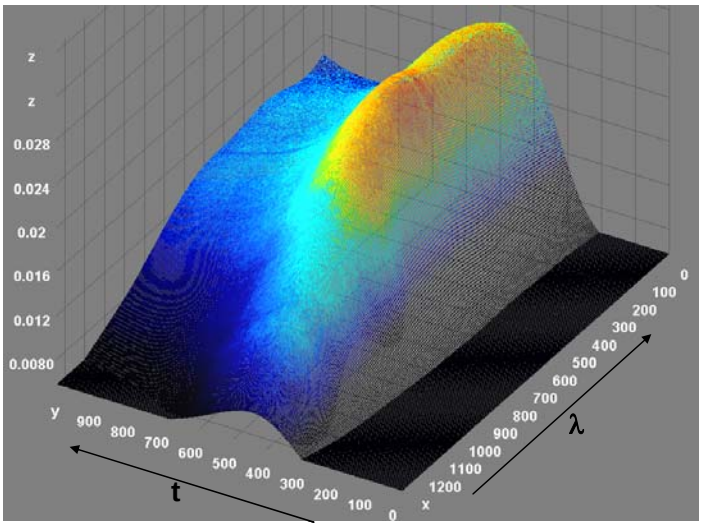

Fig. 17. 3-D plot of absolute spectrum of optical emission from heated carbon target. Time, t, is in units of 10 ns, and wavelength λ is in units of nm.

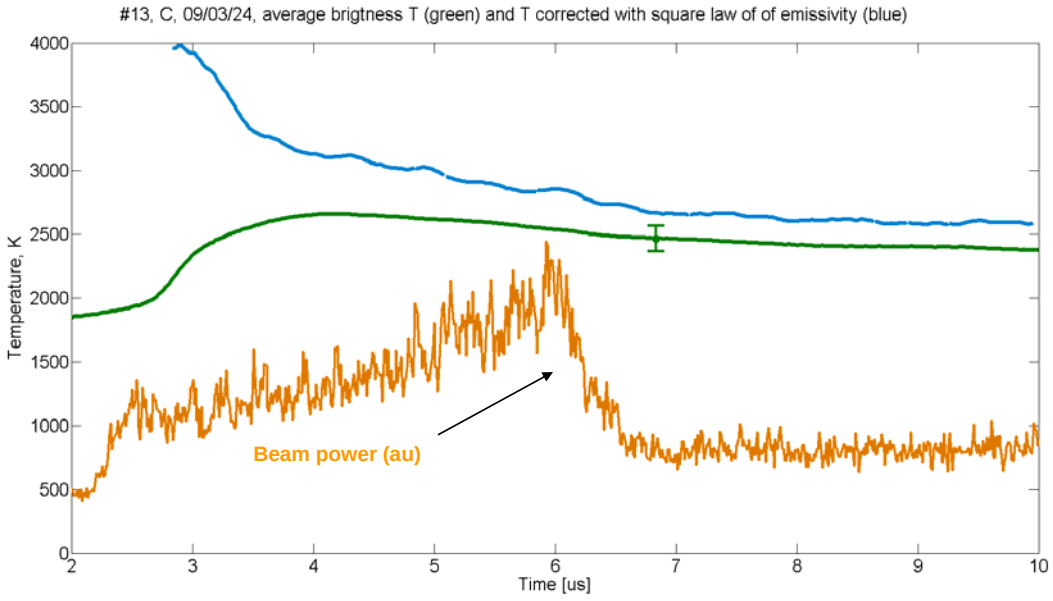

Fig. 18. Streak-spectrometer data from shot #13 (carbon target), showing the brightness temperature (green), reconstructed temperature (blue) and the optical signal at the streak-spectrometer from beam emission at the target scintillator, which is proportional to the beam power on target.

Platinum

Extensive data was taken in over 50 shots in Pt targets. The streak-spectrometer data indicates that the target temperature in platinum reaches >4000 K, in approximate agreement with model predictions. Fig. 19 shows typical streak-spectrometer data for the platinum target temperature. Note that the measured target temperature remains slightly lower than the predicted temperature. Rapid changes in target emissivity again account for differences in the brightness temperature and corrected temperature. In contrast to the Au data (below) there are no strong emission lines in the visible range for Pt vapor.

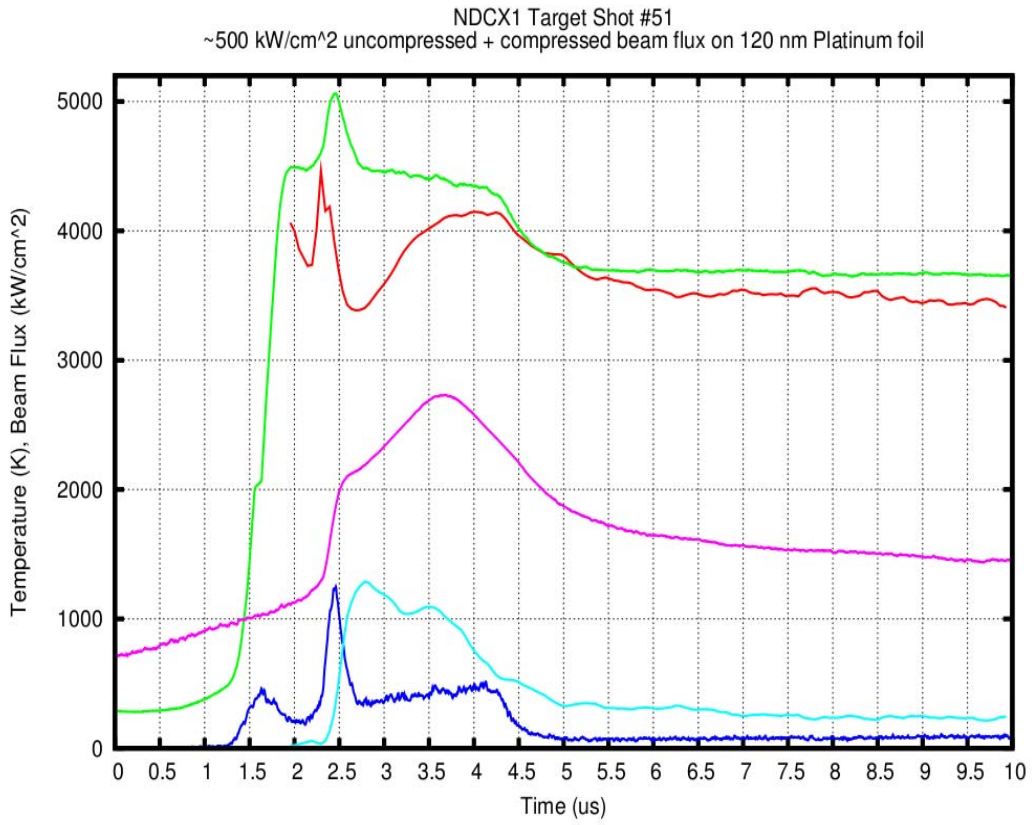

Fig. 19. Reconstructed target temperature (red) using a fit to the measured emissivity curve, brightness temperature (magenta), emissivity at 600 nm (blue), and relative time history of beam intensity (blue). The compressed pulse is timed at 1 μs after the head of the beam. Also shown is the predicted temperature behavior from the equilibrium model (green) based on the beam current pulse shown.

Fig. 20 shows optical self-emission from the expanding shower of hot debris (liquid droplets) 500 μs after the target shot. The presence of hundreds of hot droplets supports the characterization of the target as forming droplets early in the beam pulse.

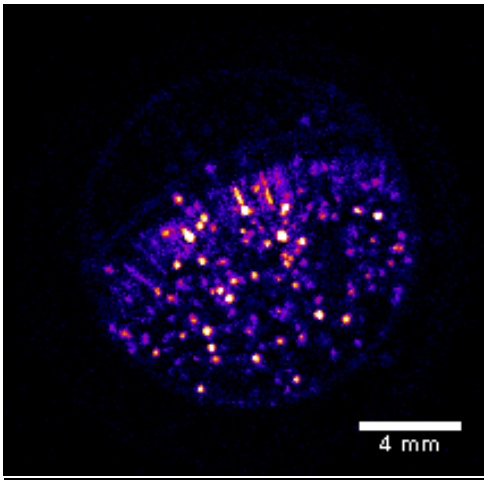

Fig. 20. Shower of hot debris (droplets) 500 μs after the beam pulse.

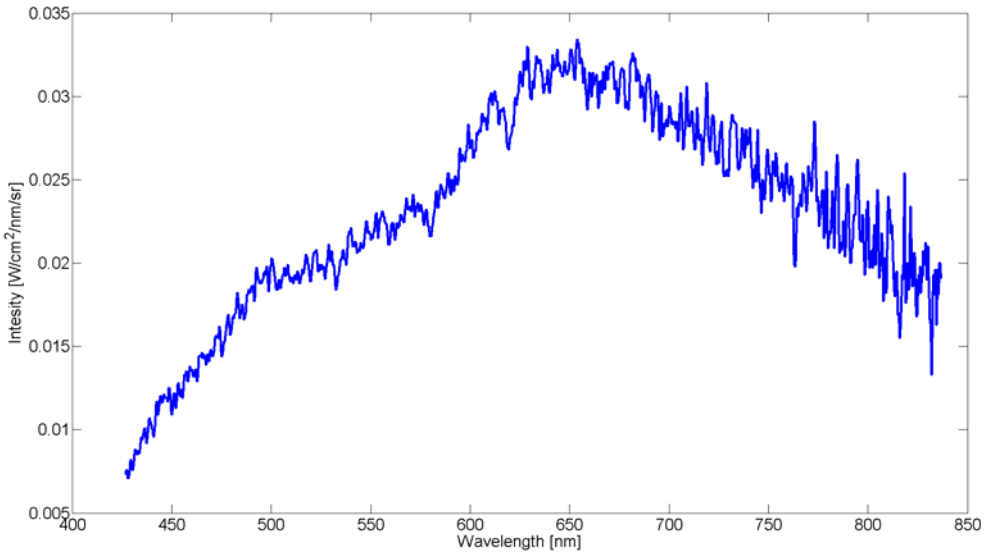

Fig. 21. Absolute radiation spectrum of Pt foil emission (t = 2 μs) showing typical fall-off of the spectrum at longer wavelength, λ > 600 nm..

The absolute radiation spectrum of Pt foil emission (Fig. 21) exhibits at certain times a fall-off at long wavelengths that is not easily explained by the Planck emission spectrum. The drop-off could be associated with droplets and may be indicative of the dynamic behavior of droplets as they form and are heated by the ion beam. A predictive model is being developed, as described above.

Gold

Summarizing over 20 shots in Au, the evolution of the Au target during and after the ion-beam-heating can be characterized by 3 distinct phases.

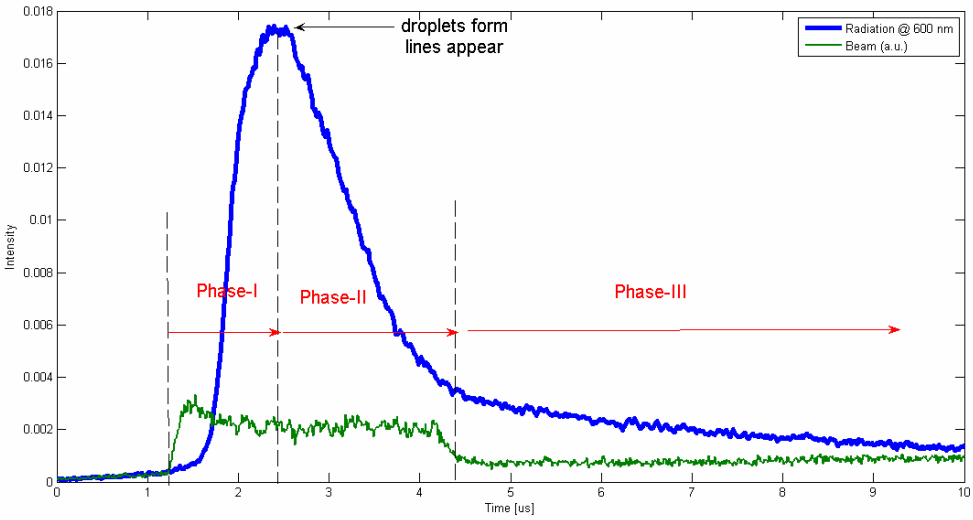

Fig. 22: Thermal radiation at 600 nm and heating-ion-beam intensity .

Phase 1

Under a continuous heating rate the thermal radiation reaches maximum after about 1.5 μs relative to the head of the beam (Figure 22). Since the ion beam is turned off later (5 μs), one would naturally expect radiation to remain at a high level during the beam pulse. This would be true if the sample remained intact during the entire heating process. However in the case of thin foils, the disassembly of a foil into droplets results in an early peak in radiation pattern. The peak in pyrometer records can be used for timing of foil disassembly.

Phase 2

Au lines appear in spectral records slightly after the radiation peaks . All gold lines were identified as Au I (atomic vapor), Figure 23.

The foil is transformed into droplets flying apart with ever increasing void. This effectively means a decrease of radiating surface area within the field of view of the diagnostic, resulting in overall decreasing of signal. Note that, while overall radiation decreases, the reconstructed temperature (from fit), gives either a constant temperature or a slight increase (beam still deposits energy into droplets), Figure 24. This is reasonable since the cooling of droplets proceeds slowly at μs time scales, and therefore temperature of droplets is effectively "locked in" and corresponds to the peak temperature before the foil disassembly.

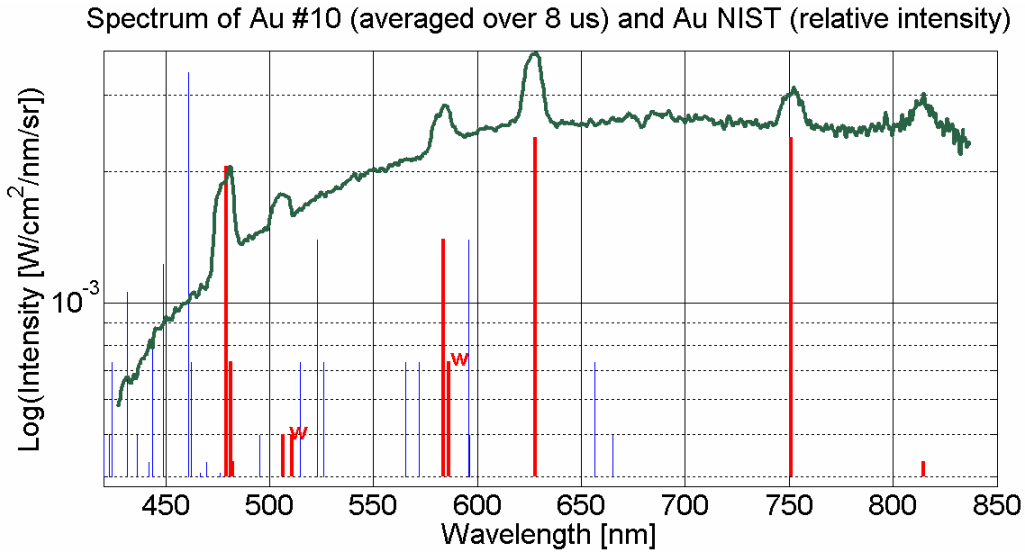

Fig. 23: Au I lines (from NIST tables) atop the continuous radiation emanating from liquid gold droplets indicate the presence of both liquid and vapor states.

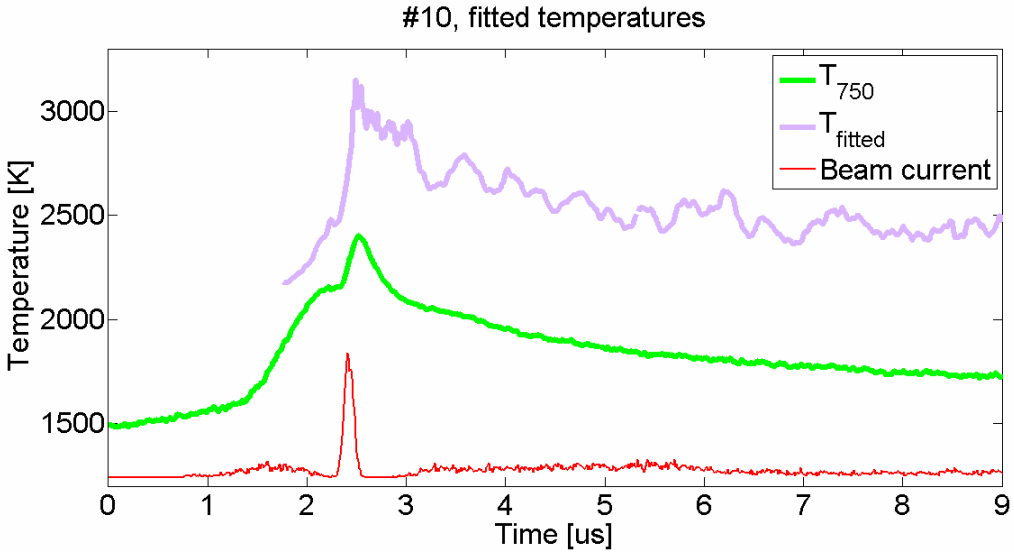

Fig. 24: Temperature reconstruction shows constant temperature after the breaking of the foil, while intensity of radiation alone decreases.

Phase 3

The radiating droplets fly apart from the field of view (400 μm circle), and the signal decreases. At later times only droplets with velocity vectors initially lying within the light collection optics aperture (22 deg) remain and therefore a nearly constant signal, i.e. "locked temperature" is detected, see Figure 22. The presence of atomic lines confirms presence of gaseous Au. This in turns leads to conclusion that the heating beam is sufficiently powerful to partially vaporize the Au sample.

Figures 25 and 26 confirm that the origin of the atomic vapor excitation is the ion beam. It follows from the fact that the intensity of the lines is modulated by the beam intensity, i.e. it disappears/decays when beam is shut off, and it increases when the compressed peak arrived.

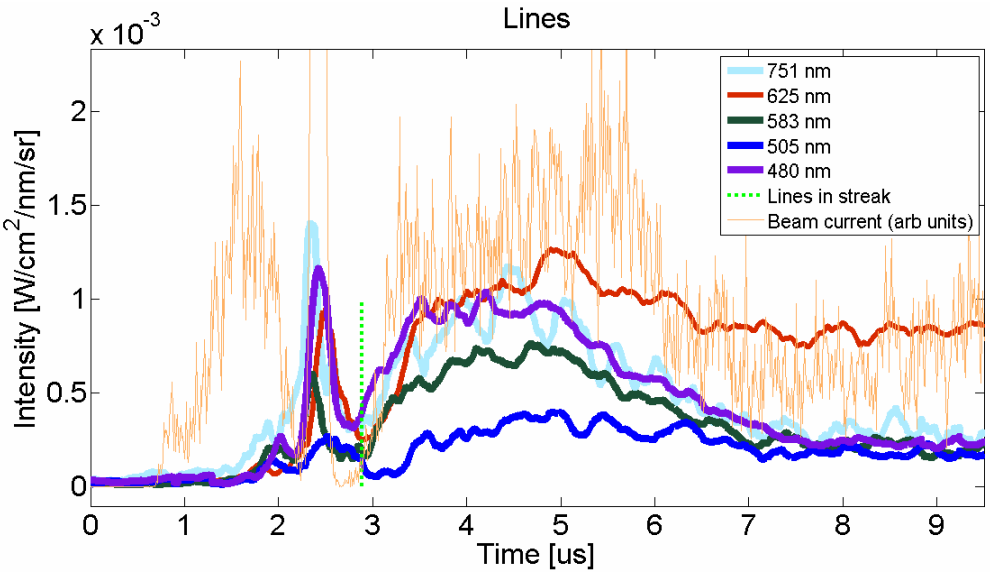

Fig. 25: Intensity of Atomic lines (continuous background subtracted) vs. beam current

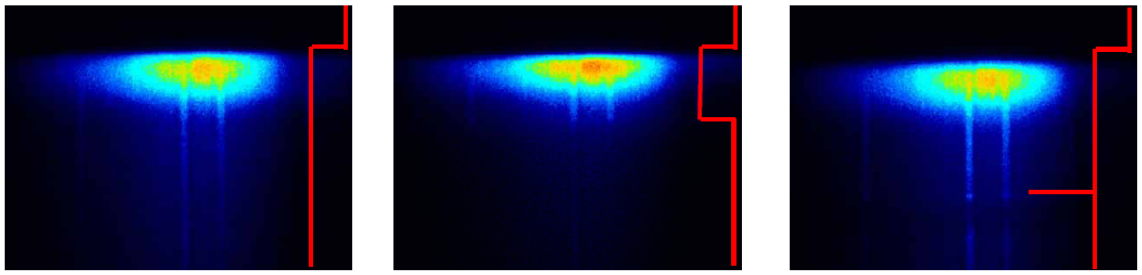

Fig. 26: Lines are modulated by beam current (schematically represented by orange lines). Time is vertical (increasing down) and wavelength is horizontal in these images.

Since the thickness of the Au target is larger than the range of ions, most of the ions are stopped in the target. Once it is agreed that lines are ion-beam-pumped, then the moment the lines appear is clearly related to breaking of the foil, i.e. ions now can pass through the void and excite the Au vapor downstream of the target.

It was mentioned before that the lines in our records start appearing slightly after the peak, which we related to the beginning of the droplet formation. Therefore Au vapor lines can also be used for tracking the droplet formation process.

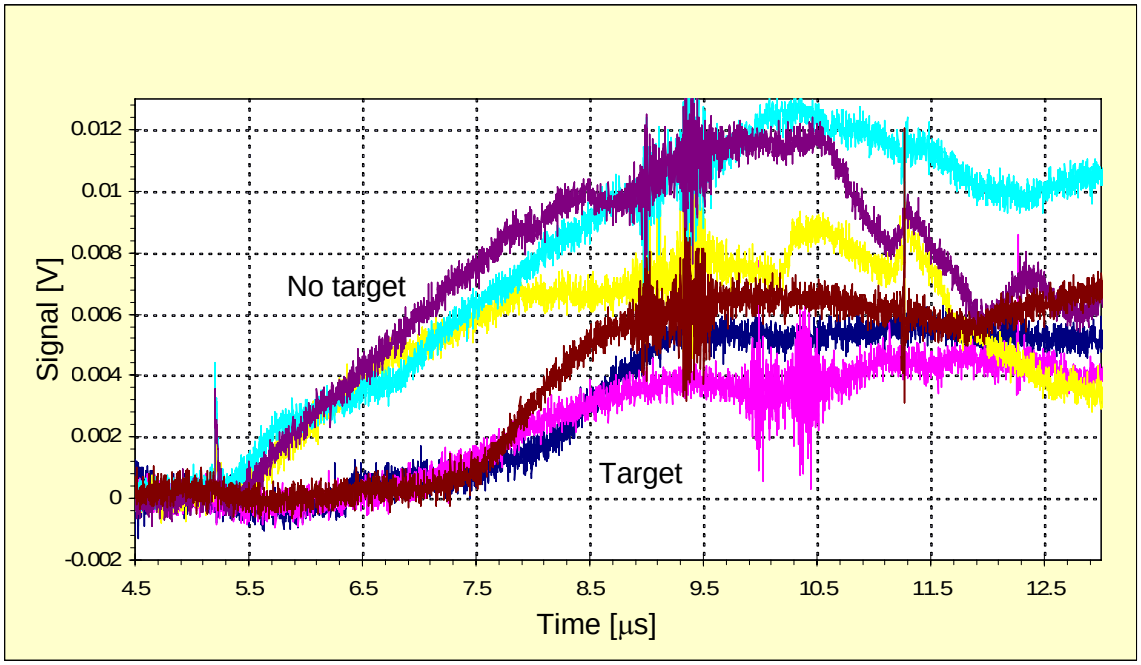

Fig. 27. Three typical current transformer signals in absence of target (signal begins rising at 5.5 μs) and three typical current transformer signals in presence of Au target (signal begins rising at 7.5 μs), showing the relative time delay at which the target begins to transmit significant ion beam current.

The current transformer downstream of the target was monitored to help verify the timing and manner of droplet formation in targets during the beam pulse (Fig. 27). The current transformer typically shows a positive current in the absence of a target foil, when the beam passes through the gold cone and the current transformer. However on a target shot the behavior of the measured current is more complicated. The transmitted current is initially small or negative downstream of the target, then typically changes sign after about 2 μs into the pulse, to approximately the level observed in the absence of the target. The observed signal is likely influenced by complicated behavior in the evolution of the target during the shot, including secondary electrons generated by the beam interacting with the target foil, electron self-emission by hot target material, and passage of beam ions through the target. However the delayed response of the current transformer signal occurs at the same time as the drop in optical radiation attributed to droplet formation as indicated by the optical diagnostics. It provides further evidence for droplet formation at this time, although the presence of the metal-vapor cloud of course provides additional beam attenuation.

7. CONCLUSIONS AND AREAS FOR FUTURE WORK

Rapid bulk heating of target foils to temperatures up to ~4500 K (0.4 eV) has been achieved using NDCX-I beams. The mechanism of target heating is described by a simple model which indicates the equilibrium between energy input from the beam and energy loss from the surface of the target due to mechanisms such as vaporization of the target material. Development of techniques for heating and diagnosing targets opens up the field of bulk heating of WDM targets in the laboratory using ion beam heating. The NDCX-I environment is conducive to multiple repetitive target experiments for detailed study of target behavior under various conditions and using multiple diagnostics.

Evidence for the formation of liquid metal droplets on the μs time scale is presented, and compared with predictions. Further experimental and theoretical work is underway in this area to improve our understanding of the mechanisms of droplet formation. The liquid-vapor transition region, and the formation of droplets is a matter of interest in WDM equation of state studies. Our experiments are expected to shed light on droplet formation in metal targets under WDM conditions and on the properties of the subsequent debris shower. These results could find wide application in areas such as
-using ion beam volumetric heating to simulate intense volumetric neutron heating, expected in inertial confinement fusion experiments, of target chamber components such as target support structures,
-optimizing applied concepts that are based on liquid metal droplets such as those, for example, for EUV photon sources for semiconductor fabrication.

Other future areas of study include the equation of state near the solid-liquid and liquid-vapor phase boundaries, and material properties such as the evaporation rate, surface tension, electrical conductivity; porous targets; positive ion/negative ion experiments in high electron affinity targets; etc.

Carbon foil targets are expected to show different behavior than metal foils and to have unusual properties compared to metals. For example, carbon foils have great strength at high temperature and are commonly used as strippers in particle accelerators. Our experiments operate at extremely high beam intensity compared to normal use in accelerators and should provide new information on the behavior and lifetime of carbon stripper foils under extreme conditions [8].

Improvements to the beamline diagnostic and targetry components will continue to be made to improve the facility for a variety of WDM experiments. We will improve the accuracy of the high voltage monitor in the induction bunching module to improve the bunching waveform tuning fidelity. We will also study the operational viability and practice of adjusting the longitudinal position of the target plane to better focus the higher energy ion beams. Further work will continue that characterize performance of the system using unipolar bunching module waveforms to compress and focus multi-energy beams.

Improvements to target diagnostics will allow improved understanding of target behavior. For example, passing a laser beam onto the target provides information on droplet formation by its effect on laser beam transmission. More detailed information, including information on the droplet size distribution may be available by observing the pattern of scattered laser light.

The NDCX I work is essential to benchmarking our beam manipulation, targetry, and diagnostic techniques for NDCX II, which will be able to probe the WDM regime at higher temperatures and pressures.

8. REFERENCES

1. HIFS-VNL 3rd Quarter 2008 milestone report, June 12, 2008.
2. J.J. Barnard, et al., Accelerator and ion beam tradeoffs for studies of warm dense matter, Proc. 2005 Particle Accelerator Conference, p. 2568
3. P.K. Roy, at al., Neutralized drift compression experiments with a high intensity ion beam, NIM A 577 (2007) 223-230.
4. P.A. Seidl, et al., Plans for longitudinal and transverse neutralized beam compression experiments, and initial results from solenoid transport experiments, NIM A 577 (2007) 215-222.
5. HIFS-VNL 4th Quarter 2008 milestone report, September 16, 2008.
6. L. D. Landau and E. M. Lifshitz, Fluid Mechanics, [Pergamon Press, Oxford], section 61, 1959.
7. P.A. Ni, M.I. Kulish, V. Mintsev, D.N. Nikolaev, V.Ya. Ternovoi, D.H.H. Hoffmann, S. Udrea, A. Hug, N.A. Tahir, D. Varentsov, “Fast six-channel pyrometer for warm-dense-matter experiments with intense heavy-ion beams”, Laser and Particle Beams, December 2008
8. S G. Lebedev and A. S. Lebedev, Phys. Rev. Spec. Top Accel. Beam. 11, 020401 (2008).